



**HAL**  
open science

## **Ferroelectric nanodomains in epitaxial GeTe thin films**

Boris Croes, Fabien Cheynis, Yide Zhang, Cédric Voulot, Kokou Dodzi Dorkenoo, Salia Cherifi-Hertel, Cristian Mocuta, Michaël Texier, Thomas W. Cornelius, Olivier Thomas, et al.

► **To cite this version:**

Boris Croes, Fabien Cheynis, Yide Zhang, Cédric Voulot, Kokou Dodzi Dorkenoo, et al.. Ferroelectric nanodomains in epitaxial GeTe thin films. *Physical Review Materials*, 2021, 5, pp.124415. 10.1103/PhysRevMaterials.5.124415 . hal-03384494

**HAL Id: hal-03384494**

**<https://hal.science/hal-03384494v1>**

Submitted on 19 Oct 2021

**HAL** is a multi-disciplinary open access archive for the deposit and dissemination of scientific research documents, whether they are published or not. The documents may come from teaching and research institutions in France or abroad, or from public or private research centers.

L'archive ouverte pluridisciplinaire **HAL**, est destinée au dépôt et à la diffusion de documents scientifiques de niveau recherche, publiés ou non, émanant des établissements d'enseignement et de recherche français ou étrangers, des laboratoires publics ou privés.

# Ferroelectric nanodomains in epitaxial GeTe thin films

Boris Croes,<sup>1</sup> Fabien Cheynis,<sup>1</sup> Yide Zhang,<sup>2</sup> Cédric Voulot,<sup>2</sup> Kokou Dodzi Dorkenoo,<sup>2</sup>  
Salia Cherifi-Hertel,<sup>2</sup> Cristian Mocuta,<sup>3</sup> Michaël Texier,<sup>4</sup> Thomas Cornelius,<sup>4</sup> Olivier  
Thomas,<sup>4</sup> Marie-Ingrid Richard,<sup>5</sup> Pierre Müller,<sup>1</sup> Stefano Curiotto,<sup>1</sup> and Frédéric Leroy<sup>1</sup>

<sup>1</sup>*Aix Marseille Univ, CNRS, CINAM, AMUTECH, Marseille, France*

<sup>2</sup>*Université de Strasbourg, CNRS, Institut de Physique et Chimie des Matériaux de Strasbourg, Strasbourg, 67000, France*

<sup>3</sup>*Synchrotron SOLEIL, L'Orme des Merisiers, St Aubin BP 48, F-91192 Gif Sur Yvette, France*

<sup>4</sup>*Aix Marseille Univ, Univ Toulon, IM2NP, AMUTECH, CNRS, F-13397 Marseille 20, France*

<sup>5</sup>*Univ Grenoble Alpes, CEA Grenoble, IRIG, MEM,  
NRS, 17 Rue Martyrs, F-38000 Grenoble, France*

(Dated: July 29, 2021)

In the quest for materials for ferroelectrics-based spintronics with a large spin-orbit coupling, it is essential to carefully control the ferroelectric domains structure, their spatial organization and the domain wall type. Here, we perform the growth of GeTe thin films on Si by molecular beam epitaxy in a large thickness range. We show that the volume fraction along with the size of the ferroelectric nanodomains can be controlled by finely adjusting the deposition thickness and temperature. We evidence the formation of 71°-type domain walls and *in situ* measurements during thermal cycling show the hysteretic appearance and decay of ferroelectric domains. In combination with a detailed analysis of the GeTe/Si interface, we demonstrate that the interfacial misfit dislocations formed during the growth plays a key role in the stability of the ferroelectric nanodomains.

PACS numbers: GeTe, ferroelectrics, domain wall

## I. INTRODUCTION

The epitaxial growth of thin films on single crystal substrates often leads to the development of strain fields. In ferroelectrics, this provides an extra degree of freedom to control their structure, ferroelectric transition temperature, and related functionalities such as optical, dielectric and piezoelectric responses [1–3]. The domain structure plays a central role in the relaxation mechanisms, owing to its strong dependence on tensile or compressive strain that is imposed by the substrate. Recently, strain engineering, by the selection of appropriate substrates, and the control of charge screening in thin films and superlattices has led to the discovery of new ferroelectric phases showing exotic domain patterns and polarization textures.[4–8] Furthermore, strain relaxation in thick films is often accompanied by the formation of ferroelastic domains and twin boundaries which can add further functionalization [9] *via* self-organized domain patterns [10–12].

Among ferroelectrics a new class of materials with high potentialities for spintronic applications has recently been introduced as ferroelectric Rashba semiconductors (FERSCs) [13 and 14]. Main results, obtained on  $\alpha$ -GeTe thin films, have demonstrated that the reversal of the ferroelectric polarization under an electric field leads to a consistent change in the spin chirality of the band structure [15 and 16]. An effective spin-to-charge conversion has also been demonstrated in a ferromagnetic-GeTe heterostructure [17 and 18] and a nonreciprocal charge transport up to room temperature has been detected [19]. All these advances pave the way for an all-electric spintronics based on semiconducting materials. However the influence of the domain structure on these phenomena still

remains unclear. Given the rhombohedral structure of GeTe (R3m space group) and the existence of an electric dipole in the (111) direction, eight possible polar domain orientations are anticipated in this system. This was unambiguously confirmed by the observation of herringbone domain configurations in low-temperature  $\alpha$ -phase GeTe crystals[20 and 21]. In the context of epitaxial (111)-oriented thin films a dominant self-poled state with a polarization perpendicular to the surface has been evidenced [15, 16, and 22]. However a few results [23 and 24] indicate that this is a simplified view and minority incursions occur in thin films. In spite of the growing interest in such ferroelectric Rashba semiconductors [25 and 26], the detailed polar domain structure and spatial organization has not been studied so far. These studies are a prerequisite for the controlled switching of ferroelectric domains and the understanding of aging properties.

In this article we address the ferroelectric nanodomains organization of  $\alpha$ -GeTe thin films grown on Si(111), the domain wall type, and the structure of the interface with the substrate. As reported by Wang et al. [23], quasi-single crystalline  $\alpha$ -GeTe thin films can be grown on Si(111) by molecular beam epitaxy using a pre-deposition of 1 monolayer (ML) of Sb onto the substrate. It is an ideal platform to study and control ferroelectric domains as they are no more limited by grain boundaries. We have determined by X-ray diffraction (three-dimensional reciprocal space maps) in combination with low energy electron microscopy (LEEM) the volume fraction of the ferroelectric domains and the domains size in a large range of film thickness (10-1800 nm). Second harmonic generation (SHG) microscopy combined to polarimetry analysis reveal the local symmetry of these domains. Using high resolution transmission electron microscopy (HR-

80 TEM) we show that domain walls are only of  $71^\circ$ -type  
 81 and that the GeTe/Si interface is stabilized by misfit dis-  
 82 locations that relax the large lattice parameter mismatch  
 83 between both lattices. The reversible decay/growth of  
 84 the ferroelectric nanodomains under annealing/cooling,  
 85 as demonstrated by *in situ* LEEM, is attributed to the  
 86 thermal stress induced by the large difference of linear  
 87 thermal expansion coefficients of both materials.

## 88 II. METHODS

### 89 Sample preparation and GeTe thin film growth by 90 molecular beam epitaxy

91 Si(111) wafers (Siltronix;  $550 \mu\text{m}$  -thick;  $\rho=1-10 \Omega\text{cm}$ )  
 92 are first cleaned by acetone and ethanol rising before  
 93 introduction in ultra high vacuum (UHV,  $P<10^{-7}$  Pa).  
 94 Then the substrates are degassed at 1000 K during 12 h  
 95 followed by repeated high temperature annealing (1500  
 96 K) during a few minutes in order to achieve a clean  $7\times 7$   
 97 surface reconstruction. Finally a deposition of 1 ML of Sb  
 98 is performed on the Si(111) surface, forming the so-called  
 99 Si(111)- $\sqrt{3}\times\sqrt{3}$ -Sb reconstruction [27] that greatly im-  
 100 proves the crystalline quality of the GeTe layer [23]. The  
 101 GeTe thin films are grown by co-deposition of Ge (1100  
 102  $^\circ\text{C}$ ) and Te (310  $^\circ\text{C}$ ) in UHV at 275 $^\circ\text{C}$  and character-  
 103 ized by *in situ* reflection high energy electron diffraction  
 104 (RHEED). All the deposition sources are effusion cells  
 105 from MBE-Komponenten.

### 106 LEEM and LEED surface characterization of 107 nanodomains

108 After growth the GeTe layers are transferred under  
 109 UHV conditions and characterized by low energy electron  
 110 microscopy and low energy electron diffraction (LEEM  
 111 III, Elmitec GmbH). LEEM images were obtained in  
 112 bright field mode at an incident energy of 26 eV where a  
 113 local maximum of reflectivity occurs. At this energy the  
 114 reflected beams by the GeTe main domain and by the  
 115 tilted ferroelectric nanodomains are clearly separated in  
 116 the focal plane. This allows to use either the medium con-  
 117 trast aperture ( $\varnothing=30 \mu\text{m}$ ) to select all reflected beams or  
 118 the smallest contrast aperture ( $\varnothing=10 \mu\text{m}$ ) to select only  
 119 the reflected beam from the main domain. In situ LEEM  
 120 characterization of the domains evolution under thermal  
 121 treatments were performed with temperature steps of  $10^\circ$   
 122 C and waiting time of 30 min for stabilization.

### 123 X-ray diffraction and 3D reciprocal space maps

124 The internal structure of GeTe thin films has been  
 125 studied by X-ray diffraction at DiffAbs beamline (Syn-  
 126 chrotron SOLEIL). X-ray diffraction data have been mea-  
 127 sured at 9.5 keV [0.13051 nm] and 16.9 keV [0.07336 nm].

128 The incident beam was focused on the sample surface  
 129 to a size of  $250 \times 300 \mu\text{m}^2$ . The diffracted intensity  
 130 was collected onto a 2D XPAD hybrid pixel detector.  
 131 Three-dimensional reciprocal space maps of the GeTe  
 132  $222_c$  Bragg reflection were recorded by rocking the sam-  
 133 ple by  $\pm 3^\circ$ . The typical step was about  $0.01^\circ$ . The data  
 134 analysis consists of a flat field correction (of the possible  
 135 non-uniform response of the various pixels of the detec-  
 136 tor) and then a conversion of the measured data from  
 137 the detector coordinates (pixel index) to diffraction an-  
 138 gles and thus to reciprocal space [28]. The 3D reciprocal  
 139 space map have been visualized finally using the Par-  
 140 aView software.

### 141 High-resolution transmission electron microscopy

142 HR-TEM investigations were performed with  $[1\bar{1}0]$   
 143 zone axis at an accelerating voltage of 300 kV on a  
 144 JEOL JEM-3010 instrument with a spatial resolution  
 145 of 0.17 nm. Using focused ion beam preparation proce-  
 146 dure (Dual beam FIB, FEI Helios 600 NanoLab), electron  
 147 transparent ultra-thin sections were extracted from the  
 148 thin films of GeTe on Si. The typical dimensions of the  
 149 electron transparent ultrathin sections are  $15 \mu\text{m}$  (length)  
 150  $\times 5 \mu\text{m}$  (height)  $\times 150-200 \text{ nm}$  (thickness). GPA analy-  
 151 sis was performed using the strain++ software applying  
 152 a mask in reciprocal space of radius  $0.8 \text{ nm}^{-1}$  producing  
 153 a lateral resolution in the images of 1.25 nm.

### 154 Second Harmonic Generation microscopy and 155 polarimetry analysis

156 Local second harmonic generation (SHG) measure-  
 157 ments were conducted by means of an inverted optical  
 158 microscope. The fundamental wave is provided by a laser  
 159 source emitting pulses of 100 fs duration at a repetition  
 160 rate of 80 MHz, centered at a wavelength  $\lambda = 800 \text{ nm}$ .  
 161 The sample was illuminated at normal incidence with  
 162 a time-averaged power of 11 mW. The SHG images are  
 163 obtained by scanning the sample with respect to the fo-  
 164 cused laser beam (objective  $\times 60$ , 0.85 numerical aperture  
 165 (NA)) using computer-controlled stepping motors. The  
 166 output intensity was spectrally filtered and collected into  
 167 a photomultiplier. Polarimetry measurements are per-  
 168 formed by recording the SHG images at different polar-  
 169 izer and analyzer angles. In the case of a a medium fo-  
 170 cusing of the fundamental beam (0.70 NA, or smaller), a  
 171 scalar model using the analytic form of SHG is sufficient  
 172 to model the local polarimetry response at polar domains  
 173 [29], domain walls.[30–32] The use of a strong focusing  
 174 (0.85 NA ) was necessary in this study to properly re-  
 175 solve the fine ferroelastic needles. In this case a vectorial  
 176 treatment of the fundamental electric field is necessary  
 177 [33]. We have thus developed a semi-analytic model for  
 178 the second harmonic polarimetry, combining the analytic  
 179 form of SHG with a vectorial modelling of the fundamen-

tal focused electric field. The as derived fitting functions take also into account the mixed character of the studied volumes (containing both *a*- and *c*-domain fractions) in both polarization plots (P-plots) and anisotropy plots (simultaneous rotation of the polarization and analyzer). The fitting functions related to both measurement geometries are presented in the Supplementary Note 1.

### III. RESULTS AND DISCUSSION

In order to determine the structure of GeTe thin films we have performed X-ray diffraction measurements. In Figure 1a, the iso-intensity surfaces of 3D reciprocal space maps [34] of GeTe epitaxial thin films close to  $222_c$  show four Bragg peaks (*c* stands for a pseudocubic unit cell). The main Bragg peak is located along the axis perpendicular to the surface and is centered at  $q_z=35.408 \text{ nm}^{-1} \pm 0.010 \text{ nm}^{-1}$ . This Bragg peak position at low  $q_z$  can be assigned to a rhombohedral distortion of GeTe thin films stretched along the [111] growth axis. In the following the real space regions giving rise to this Bragg peak are referred as *c*-domains that constitute the vast majority of the thin film. In addition three minor Bragg peaks are slightly angularly offset from this axis and localized at higher  $q_z=36.733 \text{ nm}^{-1} \pm 0.010 \text{ nm}^{-1}$ . They can be assigned to minor ferroelastic domains with a rhombohedral distortion along  $[\bar{1}\bar{1}\bar{1}]$ ,  $[\bar{1}\bar{1}\bar{1}]$  and  $[\bar{1}\bar{1}\bar{1}]$  (labelled *a*-domains). These distortions induce a rotation of the (111) crystallographic planes by  $1.36^\circ \pm 0.04^\circ$  (see Figure 1a-(iii)) and a slight compression of the (111) inter-reticular distance of 3.74% with respect to *c*-domains.

To determine the domain boundary type, the X-ray diffuse scattering around Bragg peaks provides some hints. The minor Bragg peaks from the ferroelastic *a*-domains are clearly elongated along a precise direction in reciprocal space ( $37^\circ \pm 3^\circ$  with respect to  $q_z$  axis) and this extension is more pronounced for thinner films (60 nm-thick GeTe thin film). This diffuse scattering indicates the presence of well defined interfaces between *a*- and *c*-domains and can be assigned to  $71^\circ$ -type domain walls due to finite size effect along the [110] direction (Figure 1c). TEM cross-section views (Figure 1b) show indeed that ferroelastic *a*-domains are crossing the film with sharp and straight walls perpendicular to the [110] direction. These sharp interfaces are the only one observed between the *c*-domains and *a*-domains. For the thinnest films (Figure 1a-(i)), no additional X-ray diffuse scattering is measured indicating that ferroelastic *a*-domains are independent and do not intersect each other. For thicker films, the volume fraction of ferroelastic *a*-domains increases as shown by the increase of the ratio of the integrated intensities of minor Bragg peaks with respect to the major peak (Figure 1d). This gives rise also to a more complex diffuse scattering pattern originating from the intersection area between ferroelastic *a*-domains of different variants. Experimental signatures of these in-

tersections arise from diffuse scattering bridge patterns [34 and 35] localized between ferroelastic *a*-nanodomain Bragg peaks (Figure 1a-(iii)). The center of mass of the bridges indicates a  $60^\circ$  in-plane rotation of the strain, a tilt angle of  $0.79^\circ \pm 0.05^\circ$  and an increased compression of the (111) crystallographic planes by 4.37% in the intersection area ( $q_z=36.954 \text{ nm}^{-1} \pm 0.010 \text{ nm}^{-1}$ ). Complementary X-ray diffraction measurements on non-symmetric Bragg peaks show that all the domains have a rhombohedral structure ( $a=0.429 \text{ nm}$ ,  $\alpha=58.3^\circ$ ) and that a single epitaxy exists with the Si substrate such that  $\alpha\text{-GeTe}(111)\|\text{Si}(111)$  and  $\alpha\text{-GeTe}[\bar{1}\bar{1}\bar{0}]\|\text{Si}[\bar{1}\bar{1}\bar{0}]$  [23] in pseudocubic coordinates. We can also estimate the average azimuthal misorientation between grains to be  $0.7^\circ \pm 0.2^\circ$  (Supplementary materials S1). Moreover, as shown from the threefold symmetry of the  $222_c$  Bragg peaks, the fraction of twinned grains is negligible in the layer. We estimate from the intensity of Bragg peaks that less than 5% of the layer contains twinned grains (less than 10% for the 60 nm-thick GeTe film).

In addition to the rhombohedral distortion of the GeTe unit cell, SHG microscopy combined to polarimetry analysis is a highly suited method to investigate the local symmetry and obtain the domain structure of non-centrosymmetric ferroic materials. This method is applied here to obtain the detailed domain structure of a thick GeTe film. Figure 2a shows a SHG image of a thick GeTe film revealing stripe domains superimposed to a background exhibiting a lower emission intensity. This image regroups all the domain contributions by combining three SHG images recorded at different sets of polarizer and analyser angles as explained in the Supplementary Figure S2. The observation of the fine ferroelastic stripes is made possible by a convolution mechanism in SHG microscopy involving the focused laser (Gaussian) beam and the comparatively zero-size of the nano-object like in the SHG imaging of domain walls.[32] This artificial broadening allows for the observation of the nanoscale domains and the spectral analysis of their local emission (see Supplementary Figure S3). The local polarization is derived through the precise modeling of the local SHG polarimetry (see methods) and the result is displayed in the inset of Figure 2a. The GeTe(111) films show three domain stripes oriented in-plane at  $0^\circ$  and  $\pm 120^\circ$  with a polarization oriented along the width of the stripes (see more details in Supplementary Figures S4-S6). The local SHG polarimetry confirms also the  $3m$  point group symmetry of the film and reveals a background showing out-of-plane polarization.

As these ferroelastic nanodomains meet the surface of the film they can be characterised by surface sensitive techniques, such as low energy electron microscopy (LEEM), with much higher resolution [36] (see Figure 2b-c). The LEEM contrast in reflectivity mode (bright field) shows bright and dark bands of intensity along the domains that reverse with the focusing conditions of the microscope [37] (See supplementary materials S7). This is typical feature of a ridge-and-valley morphology

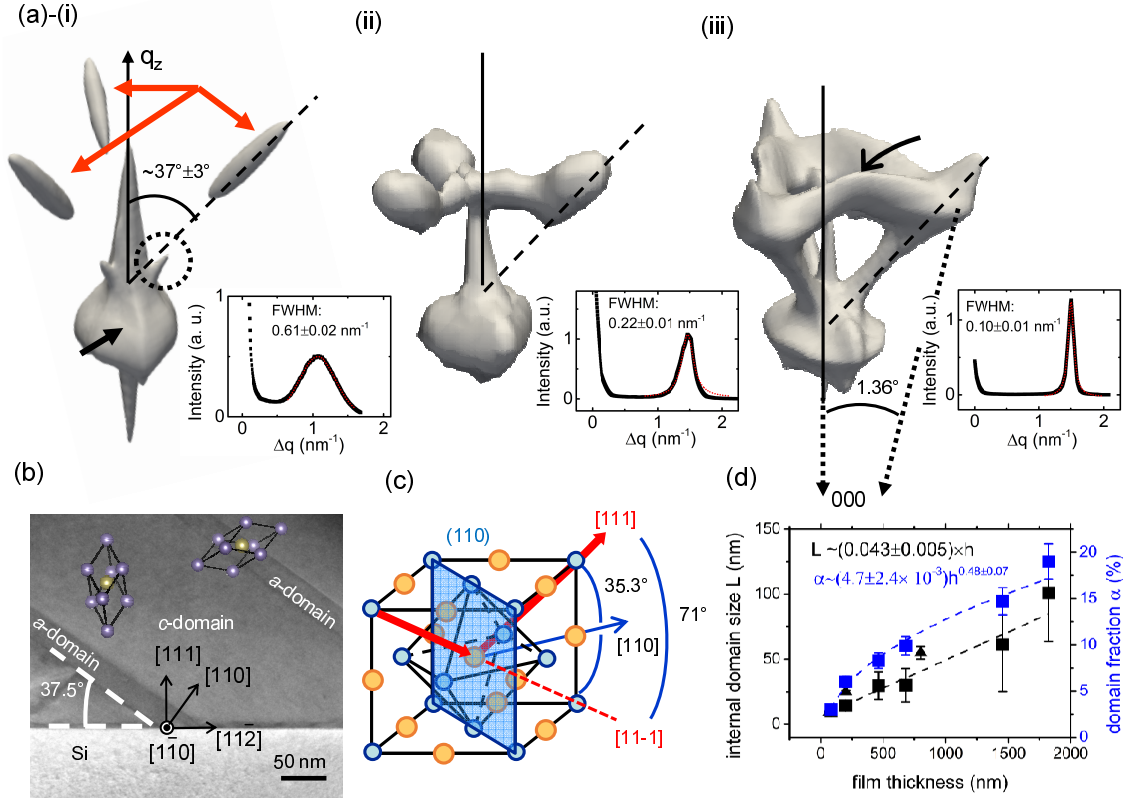


FIG. 1. (a)-(i) iso-intensity surface (2500 counts) of a 3D reciprocal space map around  $222_c$  Bragg peak of a 60 nm-thick GeTe thin film. Bragg peaks of main GeTe  $c$ -domains (black arrow) and ferroelastic  $a$ -nanodomains (red arrows). Minor ferroelastic Bragg peaks from the  $a$ -nanodomains are elongated at  $\sim 37^\circ \pm 3^\circ$  with respect to  $q_z$  axis (line profile along the dashed line in inset). Similar elongation of the diffuse scattering of GeTe  $c$ -domain (dotted circle) arising from the truncation of the  $c$ -domains by inclined  $a$ -domains (Babinet principle). (ii) and (iii) Same as (i) for a 200 nm (5000 counts) and 800 nm-thick (3000 counts) GeTe thin film. X-ray diffuse scattering bridge due to domains intersection (curved black arrow). (b) TEM cross-section of a 460 nm-thick GeTe thin film with medium resolution showing 2  $a$ -nanodomains crossing the film ( $[1\bar{1}0]$  zone axis). The rhombohedral unit cells indicates the elongation direction of the domains. (c) Scheme of the polarization (rhombohedral elongation) of the main GeTe  $c$ -domains along  $[111]$  and a secondary ferroelastic  $a$ -domain along  $[11\bar{1}]$  (in pseudocubic representation). (d) Domain size  $L$  and volume fraction  $\alpha$  of ferroelastic domains in GeTe thin films as function of film thickness deduced from the full width at half maximum of diffraction peaks of ferroelastic domains (triangle) and LEEM measurements (square).

293 and that indicates that the surface of the nanodomains  
 294 is tilted. Tilted surface patterns are characteristic fea-  
 295 tures of ferroelastic domains. The mean tilt angle of the  
 296 nanodomains has been quantitatively characterized by  $\mu$ -  
 297 LEED [38]. The reflected beams from the three domains  
 298 variants ( $0, \pm 120^\circ$ ) are slightly off-specular with respect  
 299 to the main  $(0,0)$  reflected beam (Figure 2d and inset  
 300 of Figure 2e) and the angular shift increases with the  
 301 incident electron energy  $E$  (Figure 2e). Quantitatively  
 302 the triangle area  $A$  formed by the 3 equivalent reflected  
 303 beams increases as:

$$A = \frac{18}{\sqrt{3}} \frac{m}{\hbar^2} \pi \theta^2 E \quad (1)$$

304 where  $\theta$  is the tilt angle ( $\theta \ll 1$ ),  $m$  is the electron  
 305 mass and  $\hbar$  is the reduced Planck constant. These do-

306 mains have a mean surface plane orientation that is tilted  
 307 by  $1.37^\circ \pm 0.03^\circ$  in the  $\langle 11\bar{2} \rangle$  direction with respect to  
 308 the average surface plane. These tilted planes make the  
 309 same tilt angle as the  $(111)$  crystallographic planes of  
 310 the  $a$ -nanodomains obtained from the position of the mi-  
 311 nor Bragg peaks measured by X-ray diffraction. This  
 312 unambiguously confirms the same ferroelastic origin of  
 313 the nanodomains at the surface and in the bulk of the  
 314 layer. From LEEM topographic measurements we have  
 315 also quantified the evolution of the  $a$ -domain fraction  
 316  $\alpha$  as a function of the film thickness (Figure 1d). Be-  
 317 low 30 nm, the  $a$ -domain fraction is null and the film  
 318 is therefore monodomain. Then it increases sub-linearly  
 319 [10 and 39] as  $\alpha \sim [4.7 \pm 2.4] \times 10^{-3} h^{0.48 \pm 0.07}$  ( $h$  is the  
 320 film thickness in nm). The domain width  $L$  (Figure 1d)  
 321 increases linearly over the entire range of thickness as  
 322  $L \sim [0.043 \pm 0.005] h$  nm and reaches  $\sim 77$  nm for a 1825

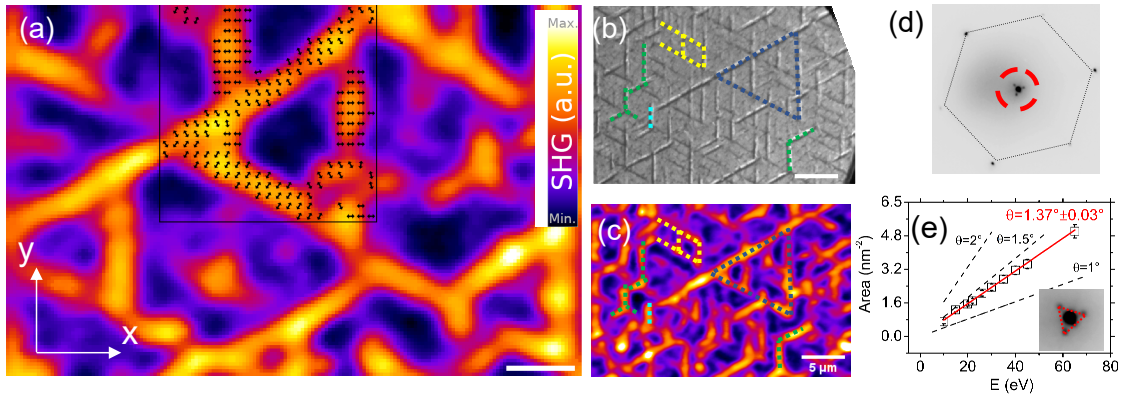


FIG. 2. (a) Isotropic second harmonic image revealing the domain structure of a 1825 nm-thick GeTe film. The black arrows indicate the local in-plane polarization orientation in the nanodomains as derived from pixel-by-pixel polarimetry analysis (see Supplementary Figure S3). The three different  $a$ -domain contributions (at  $-30^\circ$ ,  $30^\circ$  and  $90^\circ$  with respect to  $x$  axis) are superimposed to the background (dark purple) signal exhibiting out-of-plane polarisation ( $c$ -domain). The scale bar corresponds to  $2 \mu\text{m}$ . (b) LEEM image (bright field mode, incident electron energy: 26 eV) from the GeTe thin film (scale bar  $5 \mu\text{m}$ ). (c) Same area visualized by spatially resolved SHG. Dashed lines in (b) and (c) are markers. (d)  $\mu$ -LEED pattern ( $20 \mu\text{m}$  incident beam size) at 26 eV incident electron energy showing 4 reflected beams inside red dot circle: a main reflected beam and three minor beams originating from the nanodomains. (e) Area of the triangle formed by the three reflected beams (nanodomains) as function of the incident electron energy (from 8 to 65 eV). Linear fit (red line) and simulations for different tilt angles (dashed lines).

323 nm-thick GeTe film. These LEEM measurements are also  
 324 confirmed with the estimate of the  $a$ -nanodomain size  
 325 from the full width at half maximum of the diffraction  
 326 peaks of the minor domains (insets in figure 1a). The do-  
 327 main fraction and domain size results allow to evaluate  
 328 the effective period  $W = L/\alpha$  of the nanodomain pat-  
 329 tern. It reaches  $\sim 500$  nm for a 1825 nm-thick GeTe film.  
 330 Assuming in the mean strain approach [40–42] that:

$$W = \frac{\sqrt{h_0 h}}{2\xi\alpha(1-\alpha)} \quad (2)$$

331 with  $\xi = 0.27$ , we have estimated a characteristic  
 332 length  $h_0 = 0.5 \pm 0.2$  nm of the nanodomain pattern  
 333 that balances the gain of elastic energy and the costs of  
 334 domain wall and interfacial stress with the substrate.

335 The atomic scale characterization of the  $71^\circ$ -type do-  
 336 main walls and  $a$ -domains has been addressed by high-  
 337 resolution transmission electron microscopy (HR-TEM  
 338 [43]). Figure 3a shows an area including the Si substrate,  
 339 a  $a$ -domain and a  $c$ -domain separated by a  $71^\circ$ -type do-  
 340 main wall. Strain and rotation mapping of the crystalline  
 341 lattice of the GeTe layer in this area can be determined  
 342 by comparison with a reference (unstrained) region of  
 343 the Si substrate far from the interface. This has been  
 344 carried out using the image-processing technique called  
 345 the geometric phase analysis (GPA) [5, 44, and 45]. Con-  
 346 sidering that the  $x$  and  $y$  axes are respectively parallel  
 347 and perpendicular to the domain wall, we evidence that  
 348 the diagonal components of the strain tensor,  $\epsilon_{xx}$  and  
 349  $\epsilon_{yy}$ , are equal on both sides of the wall whereas the pure  
 350 shear component  $\epsilon_{xy}$  and rotation field  $\omega_{xy}$  make a signif-  
 351 icant jump across the domain wall (figure 3b). One can

352 notice that shear and rotation ( $2.2^\circ$ ) components com-  
 353 pensate across the wall to have a coplanar (110) plane as  
 354 expected from mechanical compatibility of the interface  
 355 between  $a$ - and  $c$ -domains (figure 3c) [46].

356 Ferroelastic nanodomain formation and ferroelectric  
 357 switching processes are known to be highly sensitive to  
 358 the mechanical interactions with the substrate due to the  
 359 stress induced by the lattice mismatch. This effect may  
 360 be even more pronounced for epitaxial films. To address  
 361 the relaxation mechanisms prevailing in the formation of  
 362 these ferroelastic nanodomains we have characterized the  
 363 GeTe/Si interface with HR-TEM. Figure 4a shows the in-  
 364 plane strain field ( $\epsilon_{xx}$ ) across the interface with  $x$  along  
 365  $\langle 11\bar{2} \rangle$ . The lattice parameter mismatch between the Si  
 366 substrate and the GeTe  $c$ -domain is locally  $8.2 \pm 0.2\%$  (fig-  
 367 ure 4c). In the  $a$ -nanodomain  $\epsilon_{xx}$  is larger ( $12.2 \pm 0.2\%$ )  
 368 due to the nearly in-plane stretch of the rhombohedral  
 369 distortion. Considering the lattice mismatch the forma-  
 370 tion of  $a$ -domains is elastically unfavorable if the in-plane  
 371 lattice deformation is fixed by the Si substrate lattice  
 372 parameter. However the regular modulation of the in-  
 373 plane strain component  $\epsilon_{xx}$  in GPA analysis shows that  
 374 this huge lattice parameter mismatch between the Si sub-  
 375 strate and GeTe thin film is relaxed *via* interfacial misfit  
 376 dislocations with a period of 4.10 nm (resp. 2.77 nm) for  
 377 the  $c$ -domain (resp.  $a$ -domain). This result shows that  
 378 the dislocation-assisted stress release is the main relax-  
 379 ation mechanism of the interface (see figure 4b). To com-  
 380 pare the interfacial energy cost of both GeTe  $c$ -domains  
 381 and  $a$ -domains we can make some preliminary remarks.  
 382 (i) The linear density of misfit dislocations is higher for  
 383 the  $a$ -domains ( $0.36 \text{ nm}^{-1}$ ) than for the  $c$ -domains ( $0.24$   
 384  $\text{nm}^{-1}$ ). (ii) The in-plane lattice of the  $a$ -nanodomains

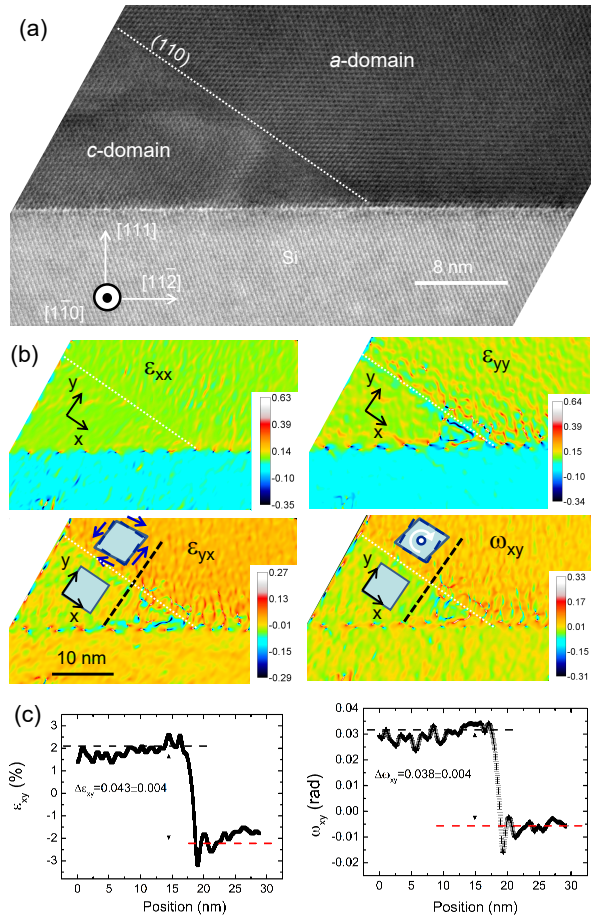


FIG. 3. (a) HR-TEM cross-section ( $\langle 1\bar{1}0 \rangle$  zone axis) of the interfacial area between the Si substrate, a GeTe  $c$ -domain and a  $a$ -nanodomain (domain wall: dotted white line) for a 460 nm-thick GeTe film. (b) In-plane  $\epsilon_{xx}$ , out-of-plane  $\epsilon_{yy}$ , shear  $\epsilon_{xy}$  strain and rotation  $\omega_{xy}$  with  $x$  and  $y$  respectively parallel and perpendicular to the domain wall. (c) Line profiles of shear and rotation across the wall (see dark dashed-line in (b)).

is monoclinic whereas it is hexagonal for the GeTe  $c$ -domains (as for the Si substrate). (iii) At last the interface plane of the  $a$ -nanodomains is expected to be tilted by  $1.36^\circ$  with respect to the Si surface plane (tilt angle of (111) plane) whereas the main GeTe  $c$ -domain and Si substrate are coplanar. Therefore the formation of the  $a$ -nanodomains appears to be energetically unfavorable.

To address the metastability of these  $a$ -nanodomains we have performed LEEM measurements during heating and cooling thermal treatments of GeTe thin films (see Supplementary Figure S8 and corresponding movie). Figure 5 shows that the ferroelastic nanodomains disappear at  $\sim 250^\circ\text{C}$ , *i.e.* slightly below the thin film growth temperature ( $275^\circ\text{C}$ ) and far below the Curie temperature ( $\sim 400^\circ\text{C}$ ). Therefore we assume that a ferroelastic configuration with only a single domain occurs during GeTe growth with a unique rhombohedral distortion

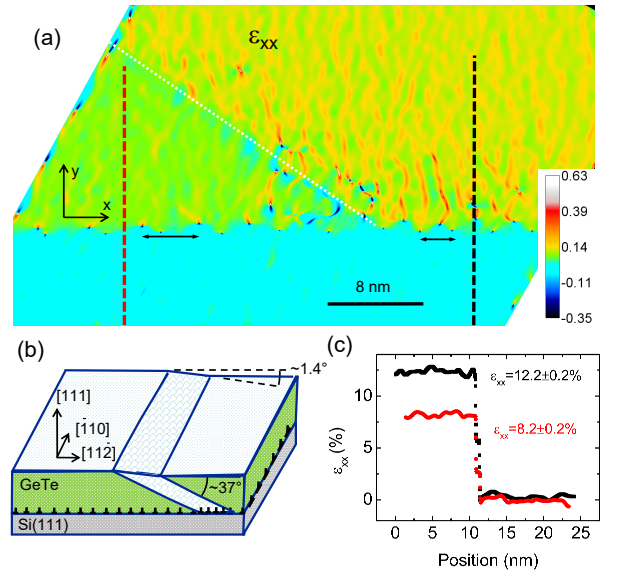


FIG. 4. (a) In-plane strain  $\epsilon_{xx}$  with  $x$  along the  $\langle 11\bar{2} \rangle$  GeTe/Si interface obtained from GPA analysis. The arrows at the GeTe/Si interface show the regular modulation of  $\epsilon_{xx}$ . (b) Model of the internal structure of GeTe thin films on Si(111). (c) Line profiles of in-plane strain  $\epsilon_{xx}$  across the interface (see dashed line in (a): dark (resp. red) line across the  $a$ -domain (resp.  $c$ -domain)).

perpendicular to the film. When cooling, the ferroelastic  $a$ -nanodomains nucleate abruptly at  $210 \pm 10^\circ\text{C}$ . This process is perfectly reproducible cycling the temperature. To explain this behaviour we infer that upon cooling a thermal stress arises due to the different linear thermal expansion coefficients of GeTe [47 and 48]  $\sim 31.9 \times 10^{-6} \text{K}^{-1}$  and Si [49 and 50]  $\sim 3.5 \times 10^{-6} \text{K}^{-1}$ . Assuming that the interfacial misfit dislocations are not enough mobile to accommodate this change [51–54] and given that GeTe lattice parameter should decrease faster than that of Si substrate, a tensile in-plane strain occurs in the GeTe layer. A very efficient way to macroscopically reduce this stress is to nucleate  $a$ -domains that expand locally the in-plane lattice parameter in the  $\langle 11\bar{2} \rangle$  direction. The three variants of the ferroelastic domains provides a global isotropic relaxation. When the GeTe layer is annealed at a temperature close to the growth temperature it recovers its growth lattice parameter, and therefore the  $a$ -nanodomains are elastically useless and spontaneously decay (see Figure 5b-c). The hysteretic behaviour of the  $a$ -domains indicates also that a nucleation energy barrier must be overpassed for their formation.

#### IV. CONCLUSION

In conclusion the domain structure of  $\alpha$ -GeTe thin films epitaxially grown on Si(111) has been investigated. By combining 3D reciprocal space mapping by X-ray

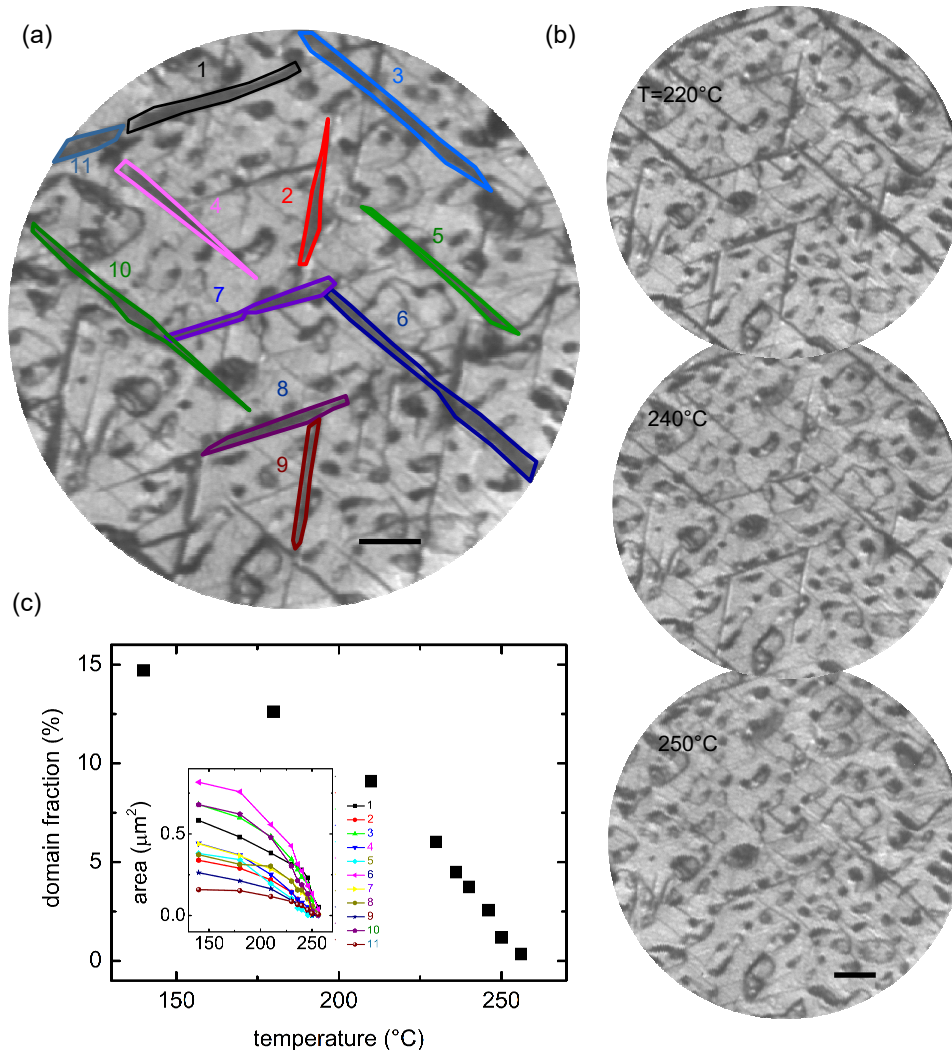


FIG. 5. (a) LEEM image (bright-field mode excluding the reflected beam from the nanodomains) of GeTe thin film (1455 nm) at 180° C. (b) Series of LEEM images at 220, 240 and 250° C. Scale bar 1  $\mu\text{m}$ . (c) Temperature evolution of *a*-nanodomains fraction as function of temperature (inset: temperature evolution of some domains area shown in (a)). The dark contrast areas that have not a needle shape correspond to local depressions in the GeTe thin film.

429 diffraction, HR-TEM, SHG and LEEM we have quan- 446  
 430 tified the volume fraction and size of the nanodomains 447  
 431 as function of the film thickness. We have demonstrated 448  
 432 that domain walls are only of 71°-type and the interface 449  
 433 with the Si substrate is stabilized by misfit dislocations 450  
 434 that relaxes the large lattice parameter mismatch. Using 451  
 435 *in situ* LEEM under cooling we have shown that the 452  
 436 ferroelectric *a*-nanodomains nucleate and grow whereas  
 437 they decay under annealing and disappear at 250 °C. 453  
 438 This result indicates that during GeTe growth at 275 454  
 439 °C, a single domain configuration occurs with a polar-  
 440 ization perpendicular to the film surface. We infer that  
 441 this single domain state during growth is a key parameter  
 442 that favors the high crystalline quality of the GeTe layer.  
 443 Then the driving force for the formation of the ferroelec-  
 444 tric nanodomains at lower temperature is attributed to  
 445 the thermal stress as the dislocations are frozen and can-

446 not accommodate the relative change of lattice parame-  
 447 ter. We believe that this detailed description of domain  
 448 behavior as a function of temperature and film thickness  
 449 will serve as a playground for the control of ferroelec-  
 450 tric/ferroelastic nanodomains in GeTe and will motivate  
 451 new strategies to tune the Rashba effect by addressing  
 452 the motion of domain walls.

#### 453 Supporting Information

454 Supporting Information is available from the Online  
 455 Library or from the author.

#### 456 Acknowledgements

457 The project leading to this publication has received  
 458 funding from Excellence Initiative of Aix-Marseille Uni-  
 459 versity A\*MIDEX, a french "Investissements d'Avenir"  
 460 programme through the AMUtech Institute. This work  
 461 has also been supported by the ANR grants HOLOLEEM



462 (ANR-15-CE09-0012) and TOPELEC (ANR-18-CE92-469  
 463 0052). S.C.-H. and C.V. acknowledge funding by the 470  
 464 LabEx NIE (ANR-11-LABX-0058-NIE) in the framework 471  
 465 of the Interdisciplinary Thematic Institute QMat (ANR- 472  
 466 17-EURE-0024), as part of the ITI 2021-2028 program 473  
 467 supported by the IdEx Unistra (ANR-10-IDEX-0002- 474  
 468 002) and SFRI STRATUS (ANR-20-SFRI-0012) through

- 475 <sup>1</sup> N. A. Pertsev, A. G. Zembilgotov, and A. K. Tagantsev. 527  
 476 Effect of Mechanical Boundary Conditions on Phase Dia- 528  
 477 grams of Epitaxial Ferroelectric Thin Films. *Physical Re-* 529  
 478 *view Letters*, 80(9):1988–1991, 1998. 530
- 479 <sup>2</sup> M. Dawber, K. M. Rabe, and J. F. Scott. Physics of 531  
 480 thin-film ferroelectric oxides. *Reviews of Modern Physics*, 532  
 481 77(4):1083–1130, 2005. 533
- 482 <sup>3</sup> J. M. Gregg. Ferroelectrics at the nanoscale. *physica status* 534  
 483 *solidi (a)*, 206(4):577–587, 2009. 535
- 484 <sup>4</sup> G. Catalan, A. Janssens, G. Rispens, S. Csiszar, O. Seeck, 536  
 485 G. Rijnders, D. H. A. Blank, and B. Noheda. Polar Do- 537  
 486 mains in Lead Titanate Films under Tensile Strain. *Phys-* 538  
 487 *ical Review Letters*, 96(12):127602, 2006. 539
- 488 <sup>5</sup> G. Catalan, A. Lubk, A. H. G. Vlooswijk, E. Snoeck, 540  
 489 C. Magen, A. Janssens, G. Rispens, G. Rijnders, D. H. A. 541  
 490 Blank, and B. Noheda. Flexoelectric rotation of polar- 542  
 491 ization in ferroelectric thin films. *Nature Materials*, 543  
 492 10(12):963–967, 2011. 544
- 493 <sup>6</sup> Tomoaki Yamada, Daisuke Ito, Tomas Sluka, Osami 545  
 494 Sakata, Hidenori Tanaka, Hiroshi Funakubo, Takahiro Na- 546  
 495 mazu, Naoki Wakiya, Masahito Yoshino, Takanori Na- 547  
 496 gasaki, and Nava Setter. Charge screening strategy for 548  
 497 domain pattern control in nano-scale ferroelectric systems. 549  
 498 *Scientific Reports*, 7(1):5236, 2017. 550
- 499 <sup>7</sup> A. K. Yadav, C. T. Nelson, S. L. Hsu, Z. Hong, J. D. 551  
 500 Clarkson, C. M. Schlepueetz, A. R. Damodaran, P. Shafer, 552  
 501 E. Arenholz, L. R. Dedon, D. Chen, A. Vishwanath, 553  
 502 A. M. Minor, L. Q. Chen, J. F. Scott, L. W. Martin, and 554  
 503 R. Ramesh. Observation of polar vortices in oxide super- 555  
 504 lattices. *Nature*, 530(7589):198+, 2016. 556
- 505 <sup>8</sup> Marios Hadjimichael, Yaqi Li, Edoardo Zatterin, Gilbert A 557  
 506 Chahine, Michele Conroy, Kalani Moore, Eoghan 558  
 507 N O’Connell, Petr Ondrejko, Pavel Marton, Jiri 559  
 508 Hlinka, Ursel Bangert, Steven Leake, and Pavlo Zubko. 560  
 509 Metal-ferroelectric supercrystals with periodically curved 561  
 510 metallic layers. *Nature Materials*, 20(4):495–502, 2021. 562
- 511 <sup>9</sup> Ekhard K. H. Salje. Ferroelastic domain walls as tem- 563  
 512 plates for multiferroic devices. *Journal of Applied Physics*, 564  
 513 128(16):164104, 2020. 565
- 514 <sup>10</sup> V Nagarajan, IG Jenkins, SP Alpay, H Li, S Aggarwal, 566  
 515 L Salamanca-Riba, AL Roytburd, and R Ramesh. Thick- 567  
 516 ness dependence of structural and electrical properties in 568  
 517 epitaxial lead zirconate titanate films. *Journal of Applied* 569  
 518 *Physics*, 86(1):595–602, 1999. 570
- 519 <sup>11</sup> A. H.G. Vlooswijk, B. Noheda, G. Catalan, A. Janssens, 571  
 520 B. Barcones, G. Rijnders, D. H.A. Blank, S. Venkatesan, 572  
 521 B. Kooi, and J. T.M. De Hosson. Smallest 90° domains 573  
 522 in epitaxial ferroelectric films. *Applied Physics Letters*, 574  
 523 91(11):20–23, 2007. 575
- 524 <sup>12</sup> L. Feigl, L. J. McGilly, C. S. Sandu, and N. Setter. Com- 576  
 525 pliant ferroelastic domains in epitaxial Pb(Zr,Ti)O<sub>3</sub> thin 577  
 526 films. *Applied Physics Letters*, 104(17):172904, 2014. 578
- 469 the French Programme d’Investissement d’Avenir. The  
 470 authors acknowledge the assistance of O. Grégut during  
 471 SHG measurements and insightful discussion about sym-  
 472 metry aspects with U. Acevedo-Salas. We are grateful to  
 473 Martiane Cabié (CP2M, Marseille) for lamella prepara-  
 474 tion of GeTe thin films by Focused Ion Beam.
- <sup>13</sup> Domenico Di Sante, Paolo Barone, Riccardo Bertacco, and  
 Silvia Picozzi. Electric Control of the Giant Rashba Effect  
 in Bulk GeTe. *Advanced Materials*, 25(4):509–513, 2013.
- <sup>14</sup> Marcus Liebmann, Christian Rinaldi, Domenico Di Sante,  
 Jens Kellner, Christian Pauly, Rui Ning Wang, Jos Emiel  
 Boschker, Alessandro Giussani, Stefano Bertoli, Matteo  
 Cantoni, Lorenzo Baldrati, Marco Asa, Ivana Vobornik,  
 Giancarlo Panaccione, Dmitry Marchenko, Jaime Sanchez-  
 Barriga, Oliver Rader, Raffaella Calarco, Silvia Picozzi,  
 Riccardo Bertacco, and Markus Morgenstern. Giant  
 Rashba-Type Spin Splitting in Ferroelectric GeTe(111).  
*Advanced Materials*, 28(3):560+, 2016.
- <sup>15</sup> Christian Rinaldi, Sara Varotto, Marco Asa, Jagoda Slaw-  
 inska, Jun Fujii, Giovanni Vinai, Stefano Cecchi, Domenico  
 Di Sante, Raffaella Calarco, Ivana Vobornik, Giancarlo  
 Panaccione, Silvia Picozzi, and Riccardo Bertacco. Ferro-  
 electric Control of the Spin Texture in GeTe. *Nano Letters*,  
 18(5):2751–2758, 2018.
- <sup>16</sup> J. Krempasky, S. Muff, J. Minar, N. Pilet, M. Fanci-  
 ulli, A. P. Weber, E. B. Guedes, M. Caputo, E. Mueller,  
 V. V. Volobuev, M. Gmitra, C. A. F. Vaz, V Scagnoli,  
 G. Springholz, and J. H. Dil. Operando Imaging of All-  
 Electric Spin Texture Manipulation in Ferroelectric and  
 Multiferroic Rashba Semiconductors. *Physical Review X*,  
 8(2), 2018.
- <sup>17</sup> C. Rinaldi, J. C. Rojas-Sanchez, R. N. Wang, Y. Fu,  
 S. Oyarzun, L. Vila, S. Bertoli, M. Asa, L. Baldrati,  
 M. Cantoni, J. M. George, R. Calarco, A. Fert, and  
 R. Bertacco. Evidence for spin to charge conversion in  
 GeTe(111). *APL Materials*, 4(3), 2016.
- <sup>18</sup> Jagoda Slawinska, Domenico Di Sante, Sara Varotto,  
 Christian Rinaldi, Riccardo Bertacco, and Silvia Picozzi.  
 Fe/GeTe(111) heterostructures as an avenue towards spin-  
 tronics based on ferroelectric Rashba semiconductors.  
*Physical Review B*, 99(7), 2019.
- <sup>19</sup> Yan Li, Yang Li, Peng Li, Bin Fang, Xu Yang, Yan Wen,  
 Dong-xing Zheng, Chen-hui Zhang, Xin He, Aurelien Man-  
 chon, Zhao-Hua Cheng, and Xi-xiang Zhang. Nonrecip-  
 rocal charge transport up to room temperature in bulk  
 Rashba semiconductor alpha-GeTe. *Nature Communica-*  
*tions*, 12(1), 2021.
- <sup>20</sup> Ho Seong Lee, Bong-Seo Kim, Chang-Woo Cho, Min-Wook  
 Oh, Bok-Ki Min, Su-Dong Park, and Hee-Woong Lee. Her-  
 ringbone structure in GeTe-based thermoelectric materi-  
 als. *Acta Materialia*, 91:83–90, 2015.
- <sup>21</sup> Paul A. Vermeulen, Anil Kumar, Gert H. ten Brink,  
 Graeme R. Blake, and Bart J. Kooi. Unravelling the Do-  
 main Structures in GeTe and LaAlO<sub>3</sub>. *Crystal Growth &*  
*Design*, 16(10):5915–5922, 2016.
- <sup>22</sup> A. V. Kolobov, D. J. Kim, A. Giussani, P. Fons, J. Tomi-  
 naga, R. Calarco, and A. Gruverman. Ferroelectric switch-  
 ing in epitaxial GeTe films. *APL Materials*, 2(6), 2014.

- 579 <sup>23</sup> Ruining Wang, Jos E. Boschker, Emilie Bruyer, Domenico 643  
 580 Di Sante, Silvia Picozzi, Karthick Perumal, Alessandro 644  
 581 Giussani, Henning Riechert, and Raffaella Calarco. To- 645  
 582 ward Truly Single Crystalline GeTe Films: The Relevance 646  
 583 of the Substrate Surface. *Journal of Physical Chemistry* 647  
 584 *C*, 118(51):29724–29730, 2014. 648
- 585 <sup>24</sup> Dominik Kriegner, Gunther Springholz, Carsten Richter, 649  
 586 Nicolas Filet, Elisabeth Mueller, Marie Capron, Helmut 650  
 587 Berger, Vaclav Holy, J. Hugo Dil, and Juraj Krempasky. 651  
 588 Ferroelectric Self-Poling in GeTe Films and Crystals. *Crys-* 652  
 589 *tals*, 9(7), 2019. 653
- 590 <sup>25</sup> Silvia Picozzi. Ferroelectric Rashba semiconductors as 654  
 591 a novel class of multifunctional materials. *Frontiers in* 655  
 592 *Physics*, 2:10, 2014. 656
- 593 <sup>26</sup> Silvia Picozzi. *Multiferroic and Ferroelectric Rashba Semi-* 657  
 594 *conductors*, pages 375–400. Springer International Pub- 658  
 595 lishing, Cham, 2020. 659
- 596 <sup>27</sup> S Andrieu. Sb adsorption on Si(111) analyzed by ellipsom- 660  
 597 etry and reflection high energy electron diffraction: Conse- 661  
 598 quences for Sb doping in Si molecular beam epitaxy. *Jour-* 662  
 599 *nal of Applied Physics*, 69(3):1366–1370, 1991. 663
- 600 <sup>28</sup> Cristian Mocuta, Marie-Ingrid Richard, Julie Fouet, Stefan 664  
 601 Stanescu, Antoine Barbier, Christophe Guichet, Olivier 665  
 602 Thomas, Stephanie Hustache, Alexey V. Zozulya, and Do- 666  
 603 minique Thiaudiere. Fast pole figure acquisition using area 667  
 604 detectors at the DiffAbs beamline - Synchrotron SOLEIL. 668  
 605 *Journal of Applied Crystallography*, 46(6):1842–1853, DEC 669  
 606 2013. 670
- 607 <sup>29</sup> Sava A. Denev, Tom T.A. Lummen, Eftihia Barnes, Amit 671  
 608 Kumar, and Venkatraman Gopalan. Probing ferroelectrics 672  
 609 using optical second harmonic generation. *Journal of the* 673  
 610 *American Ceramic Society*, 94(9):2699–2727, 2011. 674
- 611 <sup>30</sup> Salia Cherifi-Hertel, Herve Bulou, Riccardo Hertel, Gre- 675  
 612 gory Taupier, Kokou Dodzi (Honorat) Dorkenoo, Christian 676  
 613 Andreas, Jill Guyonnet, Iaroslav Gaponenko, Katia Gallo, 677  
 614 and Patrycja Paruch. Non-Ising and chiral ferroelectric do- 678  
 615 main walls revealed by nonlinear optical microscopy. *Nat-* 679  
 616 *ure Communications*, 8, 2017. 680
- 617 <sup>31</sup> Hiroko Yokota and Yoshiaki Uesu. Optical second- 681  
 618 harmonic generation microscopy as a tool for ferroelastic 682  
 619 domain wall exploration. *Journal of Applied Physics*, 683  
 620 129(1):014101, 2021. 684
- 621 <sup>32</sup> Salia Cherifi-Hertel, Cédric Voulot, Ulises Acevedo-Salas, 685  
 622 Yide Zhang, Olivier Crégut, Kokou Dodzi Dorkenoo, and 686  
 623 Riccardo Hertel. Shedding light on non-Ising polar do- 687  
 624 main walls: Insight from second harmonic generation mi- 688  
 625 croscopy and polarimetry analysis. *Journal of Applied* 689  
 626 *Physics*, 129(8):081101, 2021. 690
- 627 <sup>33</sup> K. J. Spychala, P. Mackwitz, A. Widhalm, G. Berth, and 691  
 628 A. Zrenner. Spatially resolved light field analysis of the 692  
 629 second-harmonic signal of  $\chi(2)$ -materials in the tight fo- 693  
 630 cusing regime. *Journal of Applied Physics*, 127(2), 2020. 694
- 631 <sup>34</sup> Z. L. Luo, H. Huang, H. Zhou, Z. H. Chen, Y. Yang, L. Wu, 695  
 632 C. Zhu, H. Wang, M. Yang, S. Hu, H. Wen, X. Zhang, 696  
 633 Z. Zhang, L. Chen, D. D. Fong, and C. Gao. Probing 697  
 634 the domain structure of BiFeO<sub>3</sub> epitaxial films with three- 698  
 635 dimensional reciprocal space mapping. *Applied Physics* 699  
 636 *Letters*, 104(18), 2014. 700
- 637 <sup>35</sup> J Chrosch and EKH Salje. Temperature dependence of the 701  
 638 domain wall width in LaAlO<sub>3</sub>. *Journal of Applied Physics*, 702  
 639 85(2):722–727, 1999. 703
- 640 <sup>36</sup> N. Barrett, J. E. Rault, J. L. Wang, C. Mathieu, A. Lo- 704  
 641 catelli, T. O. Montes, M. A. Niño, S. Fusil, M. Bibes, 705  
 642 A. Barthélémy, D. Sando, W. Ren, S. Prosandeev, L. Bel- 706  
 laiche, B. Vilquin, A. Petraru, I. P. Krug, and C. M. 707  
 Schneider. Full field electron spectromicroscopy applied 708  
 to ferroelectric materials. *Journal of Applied Physics*, 709  
 113(18):187217, 2013. 710
- 711 <sup>37</sup> K. M. Yu, A. Locatelli, and M. S. Altman. Compar- 712  
 ing Fourier optics and contrast transfer function model- 713  
 ing of image formation in low energy electron microscopy. 714  
*Ultramicroscopy*, 183:109–116, DEC 2017. 10th Inter- 715  
 national Workshop on Low Energy Electron Microscopy 716  
 and Photoemission Electron Microscopy (LEEM/PEEM), 717  
 Monterey, CA, SEP 11-15, 2016. 718
- 719 <sup>38</sup> WX Tang, KL Man, HC Huang, CH Woo, and MS Altman. 719  
 Growth shapes of Ag crystallites on the Si(111) surface. 720  
*Journal of Vacuum Science & Technology B*, 20(6):2492– 721  
 2495, NOV-DEC 2002. 3rd Low Energy Electron Mi- 722  
 croscopy/Photoemission Electron Microscopy Workshop, 723  
 Albuquerque, NM, MAY 14-17, 2002. 724
- 725 <sup>39</sup> WY Hsu and R Raj. X-ray characterization of the domain- 725  
 structure of epitaxial Lead Titanate thin-films on (001)- 726  
 Strontium Titanate. *Applied Physics Letters*, 67(6):792– 727  
 794, 1995. 728
- 729 <sup>40</sup> AL Roytburd. Thermodynamics of polydomain hetero- 729  
 structures. I. Effect of macrostresses. *Journal of Applied* 730  
*Physics*, 83(1):228–238, 1998. 731
- 732 <sup>41</sup> AL Roytburd. Thermodynamics of polydomain hetero- 732  
 structures. II. Effect of microstresses. *Journal of Ap-* 733  
*plied Physics*, 83(1):239–245, 1998. 734
- 735 <sup>42</sup> AK Tagantsev, LE Cross, and J Fousek. Domains in Fer- 735  
 roic Crystals and Thin Films. In *Domains in Ferroic Crys-* 736  
*tals and Thin Films*, pages 1–821. 2010. 737
- 738 <sup>43</sup> Etienne Snoeck, Axel Lubk, and César Magén. *Structural* 738  
*Characterization of Ferroelectric and Multiferroic Nano-* 739  
*structures by Advanced TEM Techniques*, chapter 10, pages 740  
 275–324. John Wiley & Sons, Ltd, 2016. 741
- 742 <sup>44</sup> MJ Hytch, E Snoeck, and R Kilaas. Quantitative mea- 742  
 surement of displacement and strain fields from HREM 743  
 micrographs. *Ultramicroscopy*, 74(3):131–146, 1998. 744
- 745 <sup>45</sup> JL Rouviere and E Sarigiannidou. Theoretical discus- 745  
 sions on the geometrical phase analysis. *Ultramicroscopy*, 746  
 106(1):1–17, 2005. 747
- 748 <sup>46</sup> Jan Fousek and Vaclav Janovec. The Orientation of Do- 748  
 main Walls in Twinned Ferroelectric Crystals. *Journal of* 749  
*Applied Physics*, 40:135–142, 1969. 750
- 751 <sup>47</sup> T Chattopadhyay, JX Boucherle, and HG Vonschering. 751  
 Neutron diffraction study on the structural phase transi- 752  
 tion in GeTe. *Journal of Physics C: Solid State Physics*, 753  
 20(10):1431–1440, 1987. 754
- 755 <sup>48</sup> Marion Gallard, Mohamed Salah Amara, Magali Put- 755  
 ero, Nelly Burle, Christophe Guichet, Stephanie Escoubas, 756  
 Marie-Ingrid Richard, Cristian Mocuta, Rebecca R. 757  
 Chahine, Mathieu Bernard, Philippe Kowalczyk, Pierre 758  
 Noe, and Olivier Thomas. New insights into thermome- 759  
 chanical behavior of GeTe thin films during crystallization. 760  
*Acta Materiala*, 191:60–69, 2020. 761
- 762 <sup>49</sup> RR Reeber and K Wang. Thermal expansion and lattice 762  
 parameters of group IV semiconductors. *Materials Chem-* 763  
*istry and Physics*, 46(2-3):259–264, 1996. 764
- 765 <sup>50</sup> H Watanabe, N Yamada, and M Okaji. Linear thermal 765  
 expansion coefficient of silicon from 293 to 1000 K. *Inter-* 766  
*national Journal of Thermophysics*, 25(1):221–236, 2004. 767
- 768 <sup>51</sup> NA Pertsev and AG Zembilgotov. Domain populations 768  
 in epitaxial ferroelectric thin films: Theoretical calcula- 769  
 tions and comparison with experiment. *Journal of Applied* 770  
*Physics*, 80(11):6401–6406, 1996. 771

- 707 <sup>52</sup> KS Lee and S Baik. Reciprocal space mapping of phase 713  
708 transformation in epitaxial PbTiO<sub>3</sub> thin films using syn- 714  
709 chrotron x-ray diffraction. *Journal of Applied Physics*, 715  
710 85(3):1995–1997, 1999. 716
- 711 <sup>53</sup> K Lee, KS Lee, and S Baik. Finite element analysis of  
712 domain structures in epitaxial PbTiO<sub>3</sub> thin films. *Journal*  
*of Applied Physics*, 90(12):6327–6331, 2001.
- <sup>54</sup> KS Lee, JH Choi, JY Lee, and S Baik. Domain formation  
in epitaxial Pb(Zr,Ti)O<sub>3</sub> thin films. *Journal of Applied*  
*Physics*, 90(8):4095–4102, 2001.